Renormalization of the valence and conduction bands of (C6H5C2H4NH3)2PbI4 hybrid perovskite

Min-I Lee, Saleem Ayaz Khan, Hela Mrezguia, Ana Barragán, Maya N Nair, Hamza Khelidj, Younal Ksari, Luca Giovanelli, Jean-Marc Themlin, Ferdinand Lédée, et al.

Renormalization of the valence and conduction bands of $(C_6H_5C_2H_4NH_3)_2PbI_4$ hybrid perovskite

Min-I Lee,[1] S. Ayaz Khan,[2] H. Mrezguia,[3] A. Barragán,[1] M. N. Nair,[1,4] H. Khelidj,[3] Y. Ksari,[3] L. Giovanelli,[3] J.-M. Themlin,[3] F. Lédée,[5] G. Trippé-Allard,[5] E. Deleporte,[5] A. Taleb-Ibrahimi,[4] J. Minár,[2] and A. Tejeda[1,*]

[1] *CNRS, Université Paris-Saclay, Laboratoire de Physique des Solides, 91405 Orsay, France*
[2] *New Technologies - Research Center, University of West Bohemia, Univerzitni 8, 306 14 Pilsen, Czech Republic*
[3] *Aix Marseille Univ, Univ Toulon, CNRS, IM2NP, Marseille, France*
[4] *Synchrotron SOLEIL, Saint-Aubin, 91192, Gif-sur-Yvette, France*
[5] *Université Paris-Saclay, ENS Paris-Saclay, CNRS, CentraleSupélec, LuMIn, 91405 Orsay, France*

Quasi two-dimensional hybrid organic-inorganic perovskites (HOIPs) have been rediscovered recently for photovoltaics due to a higher stability than other HOIPs. We focus here on the electronic structure of the 2D perovskite $(C_6H_5C_2H_4NH_3)_2PbI_4$. We perform an experimental k-resolved determination of the valence and conduction bands by angle-resolved photoemission spectroscopy (ARPES) and inverse photoemission spectroscopy (IPES). The experimental and theoretical dispersions are compared. The valence band width is in agreement with that of renormalized theoretical bands, while no significative renormalization is observed for the conduction band. The effect of the spin-orbit coupling in the conduction band is also experimentally observed.

I. INTRODUCTION

Two dimensional (2D) hybrid organic inorganic perovskites, traditionally used for optoelectronic devices[1–3], have recently attracted the attention for solar cells because of their superior stability when compared to 3D perovskites of their family[4]. 2D perovskites can indeed be associated to 3D hybrid perovskites to improve the overall stability of solar cells[5–9]. The efficiency in 2D/3D solar cells has quickly grown from 4.73% in 2014[10] to 18.97% in 2018[11]. Although these figures are smaller than in 3D solar cells, the higher stability of 2D-3D perovskite solar cells is a key factor for a potential success in commercial applications. The ultimate improvement of the efficiency requires a good understanding of the electronic structure of these materials, since the band structure controls the quantum absorption probability, the effective masses etc.

One reasonably well-known 2D perovskite is $(C_6H_5C_2H_4NH_3)_2PbI_4$, phenylethylammonium lead iodine or PEPI. The 2D structure of PEPI is derived from a 3D compound by keeping apart the inorganic lattice along c axes with their moderately sized organic cations ($C_6H_5C_2H_4NH_3^+$, PEA). When grown layer by layer, it has been shown that the lattice parameters of the ultrathin film vary depending on the different thickness. As the thickness of the ultrathin film increases from one-layer to three-layers, the lattice constant a and b expand from 8.30 Å, 8.97 Å to 8.34 Å, 9.00 Å, respectively, due to the structural relaxation[12].

The experimental electronic band gap of PEPI is reported to be around 2.56 eV[13], while the 3D prototype MAPI has 1.63 eV[14]. As a result, electronic quantum confinement is expected in 2D perovskites. The theoretical band structure of PEPI has been determined in different works[15]. Moreover, in the related perovskite 4F-PEPI, it has been pointed out that spin-orbit coupling (SOC) highly splits the electronic bands at the bottom of the conduction band[16]. This SOC effect is due to the impact of the relativistic effect from the heavy atoms in perovskites, such as lead. In addition, a giant rashba splitting has also been observed in PEPI by density functional theory and by transient spectroscopies[17]. However, despite all the interest in the PEPI perovskite, the experimental band dispersion has remained elusive.

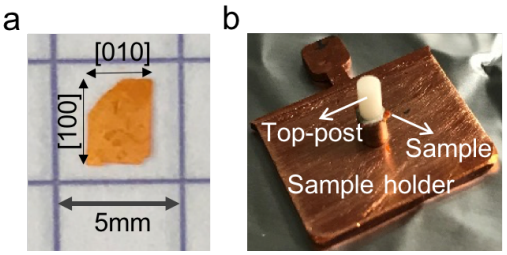

Figure 1. (a) A single crystal of PEPI, with a size of about 2.5 mm by 3 mm. (b) Sample on a sample holder with a top post attached for cleaving in ultra-high vacuum.

In this work, we report the experimental k-resolved valence and conduction bands of PEPI by angle-resolved photoemission spectroscopy (ARPES) and inverse photoemission spectroscopy (IPES). We also perform fully relativistic calculations of the band structure plus the simulation of the (inverse) photoemission process for comparing to the experimental results. In addition to the overall determination of the electronic structure, our results make explicit the experimental spin-orbit coupling effect in the conduction band as well as the renormalization of the valence band with respect to the expectations.

II. METHODS

Hybrid perovskites were prepared with the Anti-solvent Vapor-assisted Crystallization (AVC) method[18].

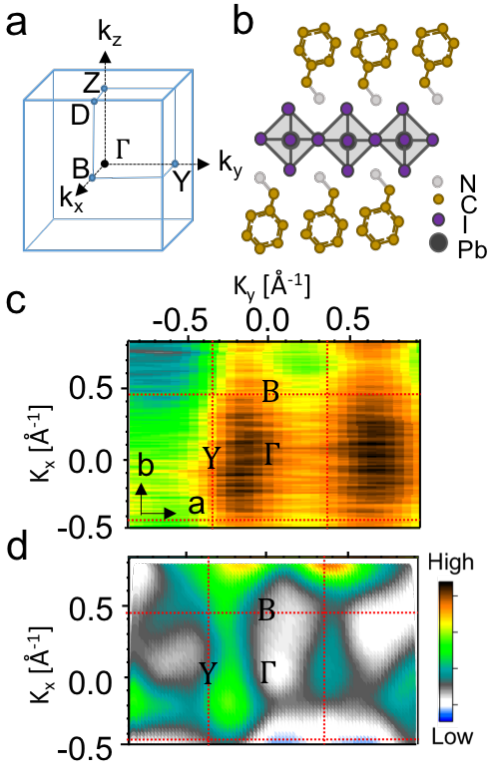

Figure 2. (a) Brillouin zone of PEPI. (b) Schematic representation of PEPI structure. (c) A standard Constant energy cut of the electronic structure at -0.5 eV below VBM, as determined (c) experimentally and (d) theoretically. The Brillouin zone is shown in (c) and (d) as red doted rectangles.

1 mol.l^{-1} solution of PbI_2 and $C_6H_5C_2H_4NH_3I$ (called PEAI hereafter) in γ-butyrolactone (GBL) (1:2 molar ratio) was poured in a small vial and placed in a bigger Teflon cap vial containing the antisolvent, i.e. dichloromethane (DCM). After 48 hours, millimeter-sized rectangle-shaped orange crystals started to grow in the small vial Fig. 1(a)).

ARPES and IPES measurements were performed after in-situ cleaving the samples under ultrahigh-vacuum conditions. Cleaving was done by hitting a top-post glued to the sample (Fig. 1(b)). ARPES measurements were carried out at the CASSIOPEE beamline of SOLEIL synchrotron, which is equipped with a high-resolution modified Petersen grating monochromator with a resolution $E/\Delta E \simeq 25,000$ below 100 eV. The analyzer is a Scienta R4000 detector with resolution $\Delta E < 1meV$ and $\Delta k \sim 0.01$Å^{-1} at $h\nu = 36eV$. IPES measurements were performed in the isochromat mode with a I_2/He Geiger-Müller type detector fitted with a CaF_2 window, detecting photons at 9.7 eV[19]. Photon counts are normalized by the absorbed current. Two codes were used for the electronic structure calculations. WIEN2k was applied to understand the effect of the organic molecule in the electronic structure. It consists of well-established full-potential linearized augmented plane wave (FLAPW) method, using a basis of density functional theory (DFT)[20]. Our calculations are based on Perdew, Burke and Ernzerhof generalized gradient approximation (PBE-GGA)[21]. The fully relativistic calculations are done by adding the spin-orbit coupling (SOC) as additional term to the scalar-relativistic Hamiltonian[22]. For the WIEN2k calculations, the crystal is divided into non overlapping muffin-tin (MT) spheres and the interstitial region between MT spheres. The wave function inside a MT sphere is expanded in terms of atomic-like wavefunctions, with the expansion controlled by the angular-momentum cutoff ($\ell_{\max}^{(\mathrm{APW})}$). In interstitial region the wave function is expanded in terms of plane waves, with the plane wave cutoff that can be controlled by the product $R_{\mathrm{MT}}K_{max}$, where R_{MT} denotes the muffin-tin sphere radius and K_{max} the magnitude of the largest wavevector. We use $\ell_{max}^{(\mathrm{APW})}$=10, R_{MT}K$_{max}$=5.0, R$_{\mathrm{MT}}$=2.5 a.u. for Pb and I, 1.37 a.u. for N, 1.27 a.u. for N and 0.69 a.u. for H atoms.

The Spin-Polarized Relativistic Korringa-Kohn-Rostoker (SPRKKR) Method[23,24] was applied to describe the angle-resolved photoemission within the one-step model originally proposed by Pendry and coworkers[25]. It is based on the KKR-Green's function that makes use of the Multiple Scattering Theory (MST). In KKR-Green function calculations, one employs a multipole expansion of the Green function for which we used a cutoff $\ell_{\max}^{(\mathrm{KKR})}$=3. Note that the cutoffs $\ell_{\max}^{(\mathrm{KKR})}$ and $\ell_{\max}^{(\mathrm{APW})}$ have different meanings in KKR and FLAPW methods, so one cannot compare their values directly. The SPRKKR use Wigner–Seitz spheres to evaluate the Green's function instead of MT spheres.

Once the Green function components (in KKR calculations) or the wave functions (in FLAPW calculations) have been determined, the charge density can be obtained via the $\boldsymbol{k}$-space integration over the Brillouin zone (BZ). The results presented in this study were obtained using an integration mesh of 600 $\boldsymbol{k}$-points for PbI_4 and PbI_4+PE in full BZ.

III. RESULTS AND DISCUSSION

The shape of the macroscopic facet (fig.1.a) allows a preliminary orientation of the single crystal. This orientation is confirmed by the periodicity of the valence band. Fig. 2b shows an experimental constant energy cut at -0.5 eV below the Valence Band Maximum (VBM). Elongated regions of high intensity are explicit, and their periodicity in the reciprocal space corresponds to 0.7 Å^{-1} which is associated to the lattice parameter a (8.984 Å, in fig. 2c). These high intensity lines correspond to equivalent directions in adjacent Brillouin zones. Moreover, since we have identified the a^* direction because of its size, we now know the orientation of the Brillouin zone in the experiment (red dotted lines). The origin of the

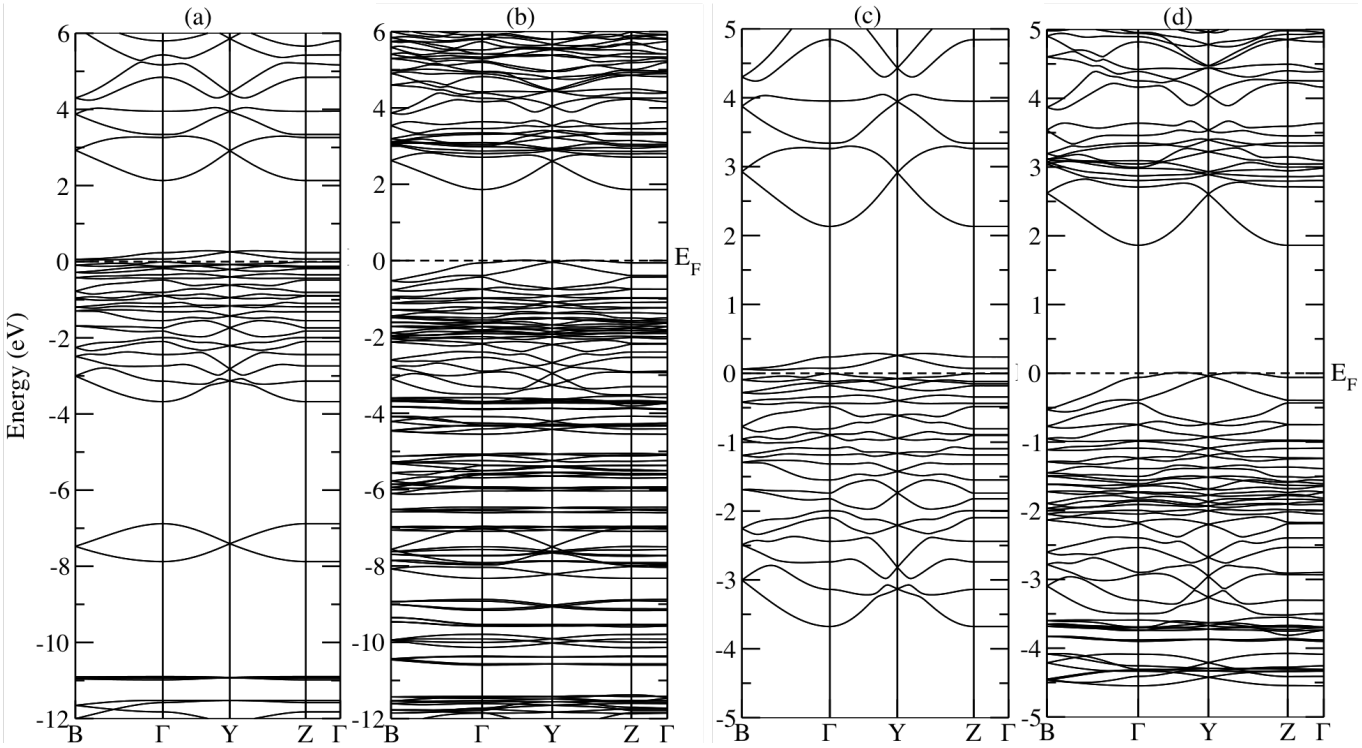

Figure 3. Theoretical band structures of inorganic and organic parts (PbI_4+PEA) considering the full structure (a, b) and zoom on (c, d).

Brillouin zone will be settled later when comparing the experiment to the theoretical bands.

Simulating photoemission measurements is a computationally demanding calculation. If we just focus on the dispersive features that can be better appreciated in the experimental measurements, we could in principle exclude phenylethylammonium $C_6H_5C_2H_4NH_3^+$ from the unit cell, that should contribute with dispersiveless molecular states. In this situation, it would be sufficient just to consider the inorganic part PbI_4 and simulate the molecular potential in the system by using empty spheres. When using the multiple scattering Green's function SPRKKR code to reproduce experimental data within the one-step model of photoemission, it is a standard procedure to introduce empty spheres in order to fillup the intersticial positions with additional scattering centers. This in particular leads to the better convergence of the scattering angular momentum expansion[31]. However, before suppressing the phenylethylammonium (PEA) molecule from the structure, we have checked the contribution to the band structure of the molecules with full Wien2K calculations.

Fig. 3 shows the results of Wien2K calculations, both for the for the PbI_4 inorganic structure only (panel a) and for the full structure including the PEA organic molecule (panel b). Zooms are shown in panels (c) and (d). It can be appreciated that the dispersing features are associated to the inorganic part, whereas molecules contribute with flat bands to the electronic structure. It can also be observed that there is no band dispersion along the ΓZ direction (perpendicular to the surface) because of the two dimensionnality of the system. Dispersing features can therefore be reproduced with the inorganic atoms, although some caution is necessary since bands are shifted in energy when suppressing the phenylethylammonium (± 0.5 eV depending on the bands). The offset between both calculations is more explicit when comparing the density of states (DOS).

Fig. 4 compares the DOS of calculations to an "experimental DOS", obtained by combining the angle-integrated PES and the IPES spectra. It can be observed that the theoretical calculation without the organic part has a lower background, although the number of spectral features with respect to the full calculation are the same, with some differences arising because of the energy shifts of the different electronic states. Such an issue is particularly visible at the minimum of the DOS between the VBM and the conduction band minimum (CBM), where there is an offset between the two calculations. Furthermore, it can be observed that even close to the Fermi level, the theoretical bands considering only the inorganic part must include an offset to compare to the experiment, that we have therefore considered in the following.

We can now identify the Brillouin zone origin in fig. 2c since the band structure calculations show that the VBM

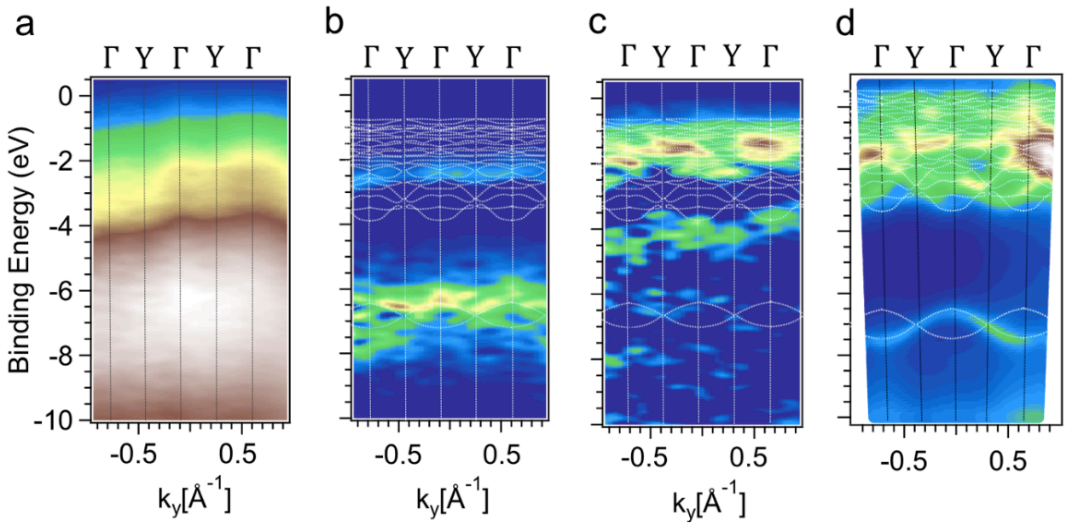

Figure 5. Experimental and theoretical ΓYΓ valence band dispersion of PEPI. (a) ARPES raw data (b) after 2D curvature analysis (c) normalized to the density of states and followed by a 2D curvature analysis. (d) Theoretical simulation of the ARPES data, with broadening the band, including SOC and considering only the inorganic part of the crystal. The theoretical band structures are superimposed on the experimental and theoretical spectra of ARPES. The flatter dispersion in the experimental results could be due to the strong electronic localization and quantum confinement in the real system.

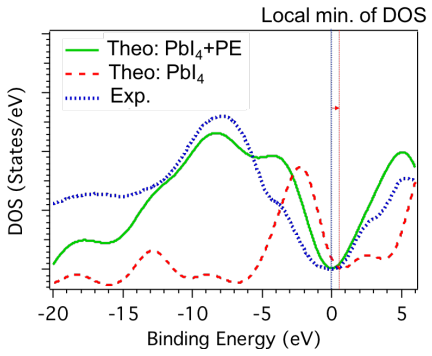

Figure 4. Density of states (DOS) of PEPI. Blue-dotted line shows the experimental DOS, green-solid line shows the calculations including the full structure, and the red-solid line shows the calculations without the organic molecules. Calculations here include a Gaussian broadening of 0.08 eV to compare to the experimental data.

takes place between Γ and Y in the absence of photoemission matrix elements (fig. 3c). It can be observed that the SPKKR calculations of the photoemission process reproduce nicely the spectral features, in particular the high-intensity vertical lines, further confirming the orientation.

Similarly, the conduction band can be determined by inverse photoemission (Fig. 6). The normalized photon yield curves along the ΓBΓ direction obtained for different electron incident angles can be analyzed together to form an image, in order to perform a similar analysis as in photoemission. Angle-dependent normalized photon yield curves already allow to observe some dispersing

Once the orientation is known, we can obtain the experimental dispersion along the in-plane high symmetry directions (fig. 5a). In order to remove the dispersiveless contribution to the $E(k)$ maps, we proceed with a 2D curvature analysis[27], as shown in fig. 5b. This treatment makes explicit the states between -6 and -8 eV although the low binding energies appearing as shoulders in the raw data are not clearly observed. If the Energy Distribution Curves are normalized by the "experimental DOS" and the 2D curvature analysis is performed afterwards, the low binding energy states (below -4 eV) appear (fig. 5c). In addition, there are some spectral features of less intensity that probably arise from the organic parts of PEPI. These experimental bands can be compared to the theoretical simulation of the spectral function (fig. 5d) that takes into account a broadening factor for the bands. This broadening can arise from the defects, that decrease the lifetime of the electronic states and therefore broaden the bands around the ideal $E_0/\Delta(E-E_0)$ position. It is clear that the theoretical bands at low binding energy are much more expanded in energy than the experimental ones, indicating a stronger electronic localization and quantum confinement in the real system. A renormalization factor is needed to be introduced in the comparison of the high-intensity features between the experiment and the theoretical calculation. features. In particular, there is a "mouth"-shaped feature originated by two dispersing bands between 1.5 and 3 eV as well as a convex spectral feature for energies between 5 and 6 eV. These are the most intense features both in the experiment (panel b) as well as in the calculation (panel c). They are well described both in its dispersion as in its intensity. Strikingly, the conduction band is not

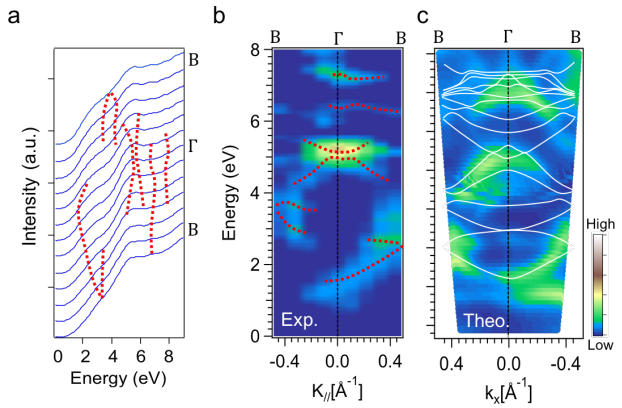

Figure 6. Experimental and theoretical ΓBΓ conduction band dispersion of PEPI. (a) Angle-dependent normalized photon yield curves. (b) Two-dimensional representation of data in (a), normalized to the density of states, followed by a 2D curvature analysis. (c) Theoretical simulation of the IPES data from a band structure calculation including SOC and considering only the inorganic part of the crystal. An offset of -1 eV is included to compare to the experiment. The calculated ground-state bands are superimposed in the E(k) images. The differences between the ground state bands and those of the simulated spectrum are attributed both to matrix element effects and to the absence of the organic part in calculations.

renormalized as it is the case for the valence band.

The band gap and the single-particle energies in semiconductors are known to renormalize due to correlation and exchange effects, as well as electron-phonon coupling. The effect on the band structure is not a simple rigid shift of the whole band structure and each valley can be renormalized differently[28]. The renormalization depends in particular on the population of the band. For instance, in the direct gap of $Al_xGa_{1-x}As$, there is a strong renormalization of the highly occupated valence band, while correlation effects in the nearly empty conduction band are minimal and the exchange correlation is negligible[28]. Dopant states that hybridize with the band can also strongly renormalize the bands, as it is known to happen for Sn or Ge doping in In_2O_3[29]. In PEPI, the valence and the conduction bands have different orbital character and can therefore give rise to different band correlations and renormalizations[30]. In fact, our GGA+U calculations allow to explain qualitatively the experimental observations, i.e. no renormalization in the empty states and normalization in the occupied states (see supplementary file). We therefore suggest that many-body effects are the reason of the renormalization of the valence band of PEPI while the conduction band remains almost fully described within the LDA approximation.

IV. CONCLUSIONS

In this work, we have determined experimentally the valence and the conduction band with wavevector resolution of phenylethylammonium lead iodine by combining angle-resolved direct and inverse photoemission. We have compared these experimental results with fully relativistic calculation of the band structure followed by the simulation of the photoemission process in a one-step model. We obtain a qualitative agreement between theory and experiment and we observe that the valence and the conduction bands need to be renormalized in a different way to describe the experimental dispersion. These results point towards an influence of many-body effects affecting mainly the valence band.

ACKNOWLEDGMENTS

We acknowledge the support from CASSIOPEE beamline staff during ARPES measurements. J. Minár is grateful for support from Computational and Experimental Design of Advanced Materials with New Functionalities (CEDAMNF; grant CZ.02.1.01/0.0/0.0/15003/0000358) of the Ministry of Education, Youth and Sports (Czech Republic) and S. A. Khan is thankful for support from GAČR (Proj. 20-18725S). This project has received funding from the European Union's Horizon 2020 programme, through an FET Open research and innovation action under Grant Agreement No. 687008. The information and views set out in this Letter are those of the authors and do not necessarily reflect the official opinion of the European Union. Neither the European Union institutions and bodies nor any person acting on their behalf may be held responsible for the use which may be made of the information contained herein.

* antonio.tejeda@u-psud.fr

[1] C. R. Kagan, D. B. Mitzi, and C. D. Dimitrakopoulos, Science, **286**, 945 (1999).
[2] K. Chondroudis, and D. B. Mitzi, Chemistry of materials, **11**, 3028 (1999).
[3] T. Hattori, T. Taira, M. Era, T. Tsutsui, and S. Saito, Chemical physics letters, **254**, 103 (1996).
[4] L. N. Quan, M. Yuan, R. Comin, O. Voznyy, E. M. Beauregard, S. Hoogland, A. Buin, A. R. Kirmani, K. Zhao, A. Amassian, and D. H. Kim, Journal of the American Chemical Society, **138**, 2649 (2016)
[5] G. Grancini, C. Roldán-Carmona, I. Zimmermann, E. Mosconi, X. Lee, D. Martineau, S. Narbey, F. Oswald, F. D. Angelis, M. Graetzel and M. K. Nazeeruddin, Nature

communications, **8**, 1 (2017).
[6] J. -C. Blancon, H. Tsai, W. Nie, C. C. Stoumpos, L. Pedesseau, C. Katan, M. Kepenekian, C. M. M. Soe, K. Appavoo, M. Y. Sfeir, S. Tretiak, P. M. Ajayan, M. G. Kanatzidis, J. Even, J. J. Crochet, and A. D. Mohite, Science, **355**, 1288 (2017).
[7] M. -H. Li, H. -H. Yeh, Y. -H. Chiang, U. -S. Jeng, C. -J. Su, H. -W. Shiu, Y. -J. Hsu, N. Kosugi, T. Ohigashi, Y. -A. Chen, P. -S. Shen, P. Chen, and T. -F. Guo, Advanced Materials **30**, 1801401 (2018).
[8] K. Wei, T. Jiang, Z. Xu, J. Zhou, J. You, Y. Tang, H. Li, R. Chen, X. Zheng, S. Wang, K. Yin, Z. Wang, J. Wang, and X. Cheng, Laser & Photonics Reviews, **12**, 1800128 (2018).
[9] P. Li, Y. Zhang, C. Liang, G. Xing, X. Liu, F. Li, X. Liu, X. Hu, G. Shao, and Y. Song, Advanced materials **30**, 1805323 (2018).
[10] I. C. Smith, E. T. Hoke, D. Solis-Ibarra, M. D. McGehee, and H. I. Karunadasa, Angewandte Chemie **126**, 11414 (2014).
[11] Y. Hu, T. Qiu, F. Bai, W. Ruan, and S. Zhang, Advanced Energy Materials **8**, 1703620 (2018).
[12] Y. -Q. Zhao, Q. -R. Ma, B. Liu, Z. -L. Yu, J. Yang, and M. -Q. Cai, Nanoscale **10**, 8677 (2018).
[13] Q. Zhang, L. Chu, F. Zhou, W. Ji, and G. Eda, Advanced Materials **30**, 1704055 (2018).
[14] M. E. Ziffer, J. C. Mohammed, and D. S. Ginger, ACS Photonics **3**, 1060 (2016).
[15] A. Fraccarollo, V. Cantatore, G. Boschetto, L. Marchese, and M. Cossi, The Journal of chemical physics **144**, 164701 (2016).
[16] J. Even, L. Pedesseau, M. -A. Dupertuis, J. -M. Jancu, and C. Katan, Physical Review B **86**, 205301 (2012).
[17] Y. Zhai, S. Baniya, C. Zhang, J. Li, P. Haney, C. -X. Sheng, E. Ehrenfreund, and Z. V. Vardeny, Science advances **3**, e1700704 (2017).
[18] F. Lédée, G. Trippé-Allard, H. Diab, P. Audebert, D. Garrot, J. -S. Lauret, and E. Deleporte, CrystEngComm **19**, 2598 (2017).
[19] V. Langlais, H. Belkhir, J. M. Themlin, J. M. Debever, L. M. Yu, P. A. Thiry., Phys. Rev. B **52**, 12095 (1995)
[20] P. Blaha, K. Schwarz, G. KH. Madsen, D. Kvasnicka, and J. Luitz, "wien2k", An augmented plane wave+ local orbitals program for calculating crystal properties (2001).
[21] J. P. Perdew, K. Burke, and M. Ernzerhof, Physical review letters **77**, 3865 (1996).
[22] A. H. MacDonald, and S. H. Vosko, Journal of Physics C: Solid State Physics **12**, 2977 (1979).
[23] H. Ebert, D. Koedderitzsch, and J. Minar, Reports on Progress in Physics **74**, 096501 (2011).
[24] H. Ebert, "The Munich SPR-KKR package, version 7.7" (2017).
[25] J. B. Pendry, Surface Science **57**, 679 (1976).
[26] M. -I. Lee, A. Barragán, M. N. Nair, V. LR. Jacques, D. Le Bolloc'h, P. Fertey, K. Jemli, F. Lédée, G. Trippé-Allard, E. Deleporte, A. Taleb-Ibrahimi, and A. Tejeda, Journal of Physics D: Applied Physics **50**, 26LT02 (2017).
[27] P. Zhang, P. Richard, T. Qian, Y. -M. Xu, X. Dai, and H. Ding, Review of Scientific Instruments **82**, 043712 (2011).
[28] H. Kalt, and M. Rinker, Physical Review B **45**, 1139 (1992).
[29] A. Walsh, J. L. F. Da Silva, and S. -H. Wei, Physical Review B **78**, 075211 (2008).
[30] A. Nicolaou, M. Gatti, E. Magnano, P. Le Fèvre, F. Bondino, F. Bertran, A. Tejeda, M. Sauvage-Simkin, A. Vlad, Y. Garreau, A. Coati, N. Guérin, F. Parmigiani, and A. Taleb-Ibrahimi, Physical Review B **92**, 081110 (2015).
[31] D. Sébilleau, K. Hatada, H. Ebert, Multiple Scattering Theory for Spectroscopies A Guide to Multiple Scattering Computer Codes, Springer (2018)